COMMUNICATIONS
CHEMISTRY

ARTICLE

https://doi.org/10.1038/s42004-019-0117-4 OPEN

Atomic palladium on graphitic carbon nitride as a hydrogen evolution catalyst under visible light irradiation

Liping Liu[1,2], Xi Wu[1], Li Wang[3], Xuejun Xu[1], Lin Gan[1], Zhichun Si[1], Jia Li[1], Qun Zhang[3], Yuxiang Liu[1], Yanyan Zhao[4], Rui Ran[2], Xiaodong Wu[2], Duan Weng[1,2] & Feiyu Kang[1,2]

Developing single-atom catalysts is extremely attractive for maximizing atomic efficiency and activity. However, the properties a nd roles of atomic catalysts in catalyzing water splitting reactions remain unclear. Here we report atomic palladium on graphitic carbon nitride with low palladium loading (0.1 wt%). The hydrogen evolution of this graphitic carbon nitride increases from 1.4 to 728 μmol g^{-1} h^{-1} under visible light irradiation, which is also 10 times higher than that of palladium nanoparticles (3 wt%) counterpart. The electronic structure of graphitic carbon nitride is modified after isolated palladium is introduced, which results in efficient charge separation, appropriate sites for adsorption for hydrogen, as well as accumulation of photoinduced electrons. Our results suggest that the pyridine nitrogen in the adjacent cavity to the palladium rather than the isolated palladium site is the active site which differs to that of the palladium nanoparticle counterpart.

---

[1] Graduate School at Shenzhen, Tsinghua University, 518055 Shenzhen City, China. [2] The Key Laboratory of Advanced Materials of Ministry of Education, School of Materials Science and Engineering, Tsinghua University, 100084 Beijing City, China. [3] Hefei National Laboratory for Physical Sciences at the Microscale, Department of Chemical Physics, Synergetic Innovation Center of Quantum Information and Quantum Physics, University of Science and Technology of China, 230026 Hefei, Anhui, China. [4] Department of Chemistry, Merkert Chemistry Center, Boston College, Chestnut Hill, MA 02467, USA. These authors contributed equally: Liping Liu, Xi Wu, Li Wang. Correspondence and requests for materials should be addressed to Z.S. (email: si.zhichun@sz.tsinghua.edu.cn) or to J.L. (email: li.jia@sz.tsinghua.edu.cn) or to Q.Z. (email: qunzh@ustc.edu.cn)

Sunlight is considered to be a desirable future energy source, with the benefits of clean, cost-free, and inexhaustible supply[1,2]. Hydrogen generation from water splitting by photocatalysts under solar light irradiation is a promising pathway to store solar energy as chemicals[1–6]. In recent decades, semiconductor photocatalysts have been widely explored to develop more efficient and less expensive photocatalysts toward solar-driven water splitting[7–9]. Among these studied catalysts, graphitic carbon nitride (C_3N_4)-based catalysts have attracted tremendous attentions due to their excellent physicochemical stability, visible-light response, metal free as well as its appealing electronic band structure ($E_g \approx 2.7$ eV) with band positions straddle the redox potentials of water splitting theoretically[8–12]. However, the fast recombination of photo-generated electron–hole pairs restricts extensive application[13]. Using noble metals as co-catalysts is an effective strategy to enhance photocatalytic efficiency of semiconductors, for which noble metals not only serve as an electron-capturing acceptors to promote the separation of photoinduced charge carriers but also act as active sites for H_2 evolution reaction[14,15]. However, high-cost and low reserves impede their practical applications. Single-atom noble metal catalysts can maximize the atom efficiency of noble metal and have high numbers of active sites for catalysis owing to their high ratio of under-coordinated metal atoms[16–18]. Importantly, the physical and chemical properties (such as bandgap and redox properties) of the catalyst will be significantly changed with the particle size of the metal being reduced to cluster or atomic scale due to the size effect[19], which results in the varied adsorption states of reactants and reduced reaction barrier for improving activity/selectivity of catalysts compared with nanoparticle catalysts[20–25]. Despite their high utilization efficiencies, single-atom catalysts need further optimization to mitigate serious aggregation or coarsening during the preparation and catalytic reaction process[26,27].

An appropriate support or ligand that strongly interacts with the noble metal atoms is required to stabilize atomic noble metals[18,28–34]. The pyridinic nitrogen atoms from bulk C_3N_4 can fix the isolated metal atoms leading to catalysts which exhibit excellent catalytic activity and product selectivity[15,32–34]. Generally, compared to Pt-based catalysts, Pd-based catalysts for water splitting are less attractive due to the fact that metallic Pd has more positive chemical potential and stronger adsorption of hydrogen. Recently, a Pd atom deposited on C_3N_4 was proved to narrow the bandgap of pristine C_3N_4 (ca. 2.7 eV) to 0.2 eV by DFT calculations[34], which indicated a promising method for obtaining long-wave solar-light responsive catalyst by loading atomic Pd or Pt on C_3N_4. Wang et al.[9] developed a reduced bandgap and promoted charge separation of polymeric photocatalyst of C_3N_4 by O doping, resulting from the unique structure with both oxygen linkers and nitrogen linkers. Gao et al.[35] reported that the binding free energy of hydrogen atom on C_3N_4 is very sensitive to mechanical strain. They replaced a bridging carbon atom in C_3N_4 with an isoelectronic silicon atom to induce mechanical strain, and then attained a zero of binding free energy of hydrogen on C_3N_4, which is favorable for the H_2 evolution[35]. Very recently, Cao et al.[15] found that both interlayers intercalated and surface-anchored Pd atoms presented in an atomic Pd/C_3N_4 layer material. This unique structure provided the driving force for the directional charge-transfer in both vertical and in-plane transportation via Pd atoms and the surface Pd atoms served as reactive sites. However, the surface Pd atoms with various oxidation states strongly indicated a complex state of Pd atoms on C_3N_4, which disturb the analysis of the role of Pd in water splitting. Additionally, the superior performance and reaction route of atomic Pd/C_3N_4 in comparison with benchmark catalysts based on different Pd sizes (i.e., nanoparticles and clusters) have not been revealed yet.

In this work, we investigate the catalytic properties of atomic Pd on bulk C_3N_4 catalyst and its roles in catalyzing water splitting reactions in comparison with benchmark catalysts with different Pd particle sizes. Especially, a distinctive reaction route of photocatalytic H_2 evolution is clarified in our study that the pyridine N in the C_3N_4 cavity adjoining Pd-loaded cavity rather than Pd atom is the active site of atomic Pd/C_3N_4. This finding presents insights into the roles of pyridine N in the cavities of C_3N_4 with decorated heteroatoms in H_2 evolution process and may give inspiration for designing and investigating atomic catalysts for water splitting on which the reaction mechanism may be distinct from those on nanoparticle or cluster catalysts.

Results

Identification of single-atom catalyst. The bulk C_3N_4 powder was prepared via thermal condensation of urea[36]. The Pd/C_3N_4 catalysts were synthesized using a facile liquid-phase adsorption–deposition method, denoted *x*Pd/C_3N_4 in which *x* stands for the Pd loading amount in weight (e.g., 0.1 Pd/C_3N_4 means that the Pd loading amount is 0.1 wt%). The textural properties of catalysts are shown in Supplementary Tables 1 and 2. As depicted by the X-ray diffraction (XRD) results (Supplementary Figure 1), all catalysts display similar patterns with a typical C_3N_4 structure and no signals assignable to palladium species can be found. The high angle annular dark field (HAADF) scanning transmission electron microscopy (STEM) graphs of the prepared Pd/C_3N_4 photocatalysts are shown in Fig. 1a–d. As for 3 Pd/C_3N_4, most of Pd species exist as spherical nanoparticles with average size of 2–3 nm and the lattice fringes with *d* spacing of 0.23 nm, which are in good agreement with Pd (111) (JCPD 65-2867). As for 0.1 Pd/C_3N_4, no nanoparticles or large clusters can be observed (Fig. 1c); instead, the high-resolution STEM image in Fig. 1d suggests the presence of isolated Pd, as indicated by the white arrows.

EXAFS spectrum of the 0.1 Pd/C_3N_4 catalyst is depicted in Fig. 1e and the related results are summarized in Supplementary Table 3. No peaks ascribed to bulk Pd phase (~2.7 Å) can be detected[37,38]. Moreover, a single sharp peak at about 1.6 Å (not phase-corrected) appears in the EXAFS spectrum of the 0.1 Pd/C_3N_4, which is ascribed to the Pd–C/N bond[33]. This result corroborated the atomic distribution of Pd in 0.1 Pd/C_3N_4. Generally, EXAFS cannot distinguish the coordinated C and N atoms, because they give similar scattering parameters due to their neighboring positions in the periodic table of elements. Several previous works reported the preferential coordination of Pd atom to nitride rather than carbon when palladium is loaded on nitrogen-doped carbon[39,40]. To consolidate the coordinated station of Pd with N atoms, we employed the density-functional theory (DFT) method to optimize the most stable adsorption sites for atomic Pd on C_3N_4, and the results turned out to be consistently well with the EXAFS results (discussed later).

Photocatalytic H_2 evolution performance. Considering that the UV light only accounts for about 5% of the total solar energy, which is far less than the visible-light (~43% of solar spectrum)[41]. For this reason, we evaluated the photocatalytic H_2 evolution under visible light irradiation. It is seen from Fig. 1f that the pristine C_3N_4 shows rather poor H_2 production (1.4 μmol g^{-1} h^{-1}). When introducing 0.05 wt% of Pd on C_3N_4, the H_2 evolution is dramatically enhanced to 435.3 μmol g^{-1} h^{-1}. With increasing the Pd loading amount, the H_2 evolution rate firstly increase and then decrease after a threshold. The optimal H_2 evolution rate is up to 728 μmol g^{-1} h^{-1} on 0.1 Pd/C_3N_4 catalyst

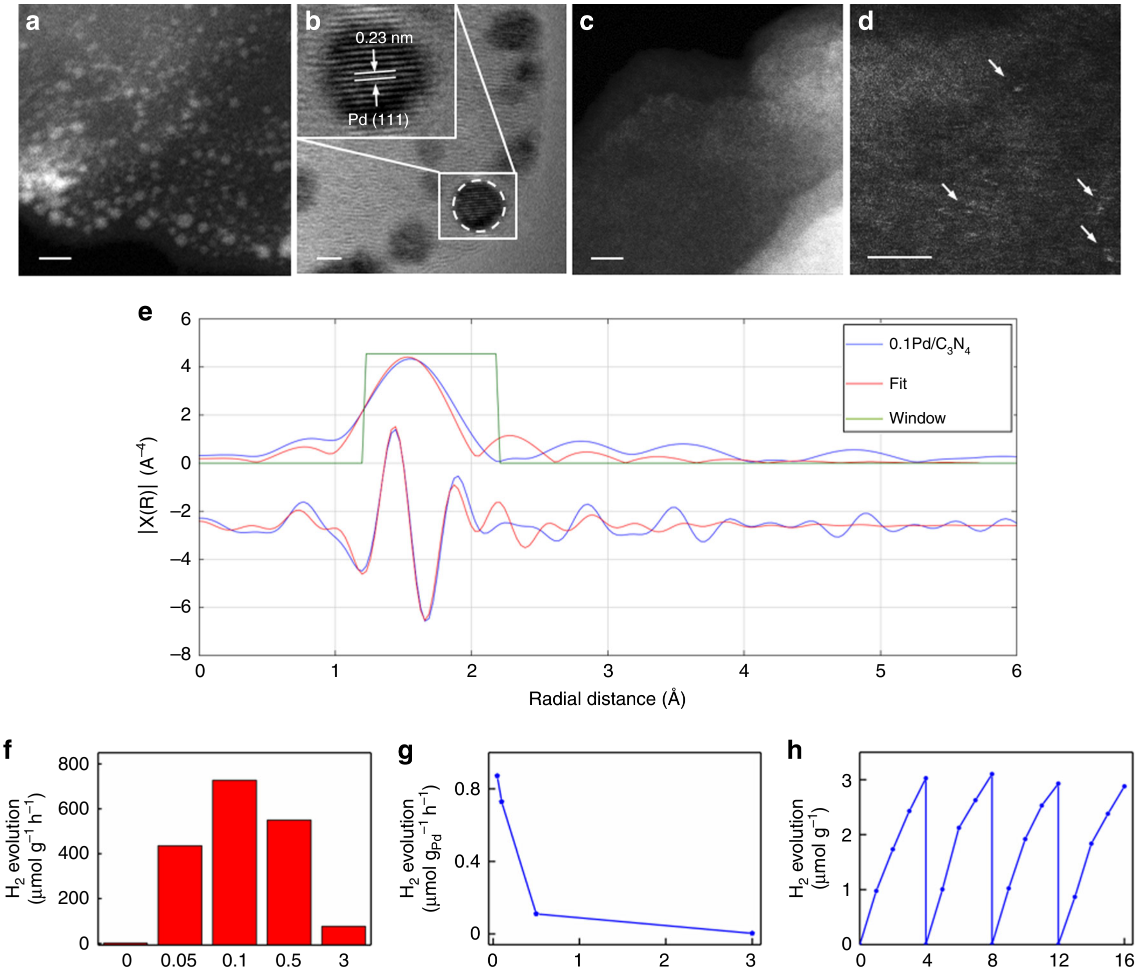

Fig. 1 Microstructure and H_2 evolution performance of catalysts. **a** HAADF-STEM image and **b** HRTEM image of 3 Pd/C_3N_4. In **b**, the dotted circle refers to Pd nanoparticle; the inset shows the enlarged area from white box region and the crystalline interplanar spacing of Pd nanoparticle is marked by white lines, showing a typical *d* spacing of 0.23 nm ascribed to Pd (111). HAADF-STEM images of 0.1 Pd/C_3N_4 **c** without and **d** with detected Pd. The white arrows in **d** denote the single Pd atoms. Scale bars: **a**, **c** 5 nm; **b**, **d** 2 nm. **e** EXAFS spectrum of 0.1 Pd/C_3N_4. **f** Photocatalytic H_2 evolution performances measured by per gram weight of catalysts. **g** H_2 evolution measured by per gram of Pd. **h** Cycling test of H_2 evolution activity over 0.1 Pd/C_3N_4

which is remarkably higher than the reported activity of Pd catalyst (326 μmol g^{-1} h^{-1})[42]. Besides, we also calculated the activities on per milligram Pd, these corresponding activities of *x*Pd/C_3N_4 catalysts monotonically increase with decreasing the Pd loading amounts. The 0.05 Pd/C_3N_4 and 0.1 Pd/C_3N_4 catalysts have similarly much higher turn over frequency (TOF). These results indicate that the single Pd atoms interacting with C_3N_4 are the most active sites on *x*Pd/C_3N_4 catalyst. CO pulse chemisorption measurements were also introduced to access the metal dispersion. However, different from conventional Pd catalysts, atomic 0.1 Pd/C_3N_4 exhibited no CO uptake, which was further verified by Fourier transform infrared spectroscopy (FTIR, Supplementary Figure 2). This phenomenon suggests that isolated Pd-based catalyst behaves differently from those conventional Pd-based catalysts, in accordance with the recent work by Pérez-Ramírez[33]. From Fig. 1g, one can see that the 0.1 Pd/C_3N_4 catalyst after running four cycles does not exhibit apparent deactivation, suggesting the good stability during H_2 evolution reaction under visible light irradiation. which has been further confirmed by the HAADF-STEM images of the used sample (only isolated Pd can be found) in Supplementary Figure 3b.

Experimental characterization of catalysts. In an attempt to unravel the mechanism behind the aforementioned change between palladium content and H_2 evolution performance, we resorted to femtosecond time-resolved transient absorption (fs-TA) spectroscopy, a robust tool for tracking the time-resolved photoexcited electron dynamics of nanosystems[32,43,44]. The samples under investigation were 0.1 Pd/C_3N_4, 0.5 Pd/C_3N_4, and 3 Pd/C_3N_4, apart from the bare C_3N_4 as a reference. In the fs-TA measurements, a pump-probe scheme with an ultraviolet pump and a white-light continuum probe was adopted. The center wavelength of the pump was chosen at 400 nm, which is effective for promoting electrons from the valence band to the conduction band of C_3N_4. Since the 450–650 nm probe was found to produce essentially the same fs-TA kinetics for each sample, we show here a representative set of data taken at 520 nm (Fig. 2a). All of the fs-TA signals manifested as negatively valued photoinduced bleach and their recovery can be well described by a bi-exponential function: $\tau_1 = 0.14 \pm 0.01$ ps (66%) and $\tau_2 = 8.5 \pm 0.5$ ps (34%) for C_3N_4, $\tau_1 = 0.30 \pm 0.05$ ps (47%), and $\tau_2 = 13.7 \pm 1.4$ ps (53%) for 0.1 Pd/C_3N_4, $\tau_1 = 0.28 \pm 0.03$ ps (63%) and $\tau_2 = 7.8 \pm 0.7$ ps (37%) for 0.5 Pd/C_3N_4, $\tau_1 = 0.29 \pm 0.03$ ps (58%) and $\tau_2 = 5.3 \pm 0.5$ ps (42%) for 3 Pd/C_3N_4. On average, the mean recovery lifetimes ($\langle\tau\rangle$) are 2.98 ± 0.18, 7.40 ± 0.77, 3.06 ± 0.28, and 2.39 ± 0.23 ps for C_3N_4, 0.1Pd/C_3N_4, 0.5Pd/C_3N_4, and 3Pd/C_3N_4, respectively, as plotted in Fig. 2b. Remarkably, 0.1Pd/C_3N_4 stands out with a longest mean recovery lifetime, which is roughly 2.5-

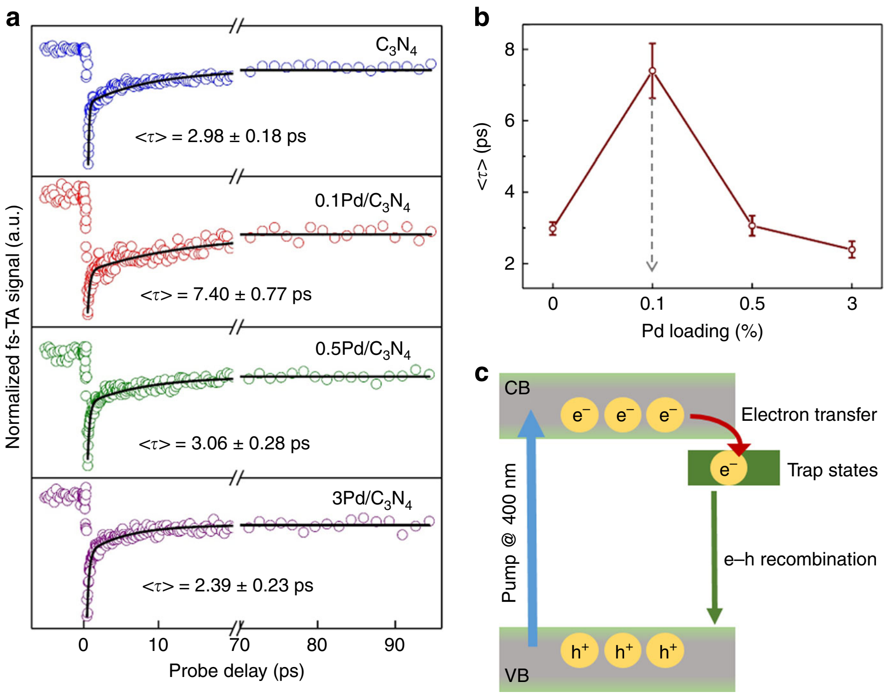

Fig. 2 Charge-transfer characterization of fs-TA. **a** Representative fs-TA kinetics recorded on C_3N_4, 0.1Pd/C_3N_4, 0.5Pd/C_3N_4, and 3Pd/C_3N_4. Pump: 400 nm; probe: 520 nm. **b** The mean recovery life time as a function of the Pd loading amount. The gray dashed arrow denotes the Pd loading amount of the catalyst which stands out with the longest mean recovery lifetime. The error bars are determined from the chi-square values obtained in the fit. **c** A plausible mechanism underlying the involved photophysical processes

fold of that observed in bare C_3N_4 (i.e. 7.4 ps for 0.1Pd/C_3N_4 vs. 2.98 ps for C_3N_4), echoing well to the volcano-shaped relationship in Fig. 1f. Additionally, both photocurrent response (PC) and electrochemical impedance spectra (EIS) measurements (Supplementary Figure 4) were performed. 0.1Pd/C_3N_4 exhibits the highest photocurrent intensity and smallest interfacial charge transfer impedance, suggesting that 0.1Pd/C_3N_4 possesses more efficient charge separation and faster charge transfer than other catalysts, which are consistent with the fs-TA results. Similar to our previous investigation on the single atomic Pt/C_3N_4 system[32], in this particular case of 0.1Pd/C_3N_4 the addition of isolated single Pd atoms into the C_3N_4 network may turned out to induce a pronounced intrinsic change of the near band-edge electron trap states of C_3N_4 (Fig. 2c) in such a way that the longer-lived photogenerated electrons can have more opportunities to participate in the H^+ reduction, leading to its best performance of photocatalytic H_2 evolution among others. Cao et al.[15] clarified that the interlayer intercalated isolated Pd atoms could provide a vertical channel for directional charge transfer from the bulk to the surface via DFT calculation, which is also benefit for the efficient charge separation.

X-ray photoelectron spectroscopy (XPS) were employed to confirm the material structure and chemical state, and the related results are depicted in Supplementary Figure 5. Etching with an Ar^+ beam was conducted to remove surface layers to obtain access to the bulk composition of the material. Like the results from Cao et al.[15] part of Pd atoms are incorporated into the subsurface of C_3N_4 were found after Ar^+ etching. Consequently, the presence of interlayer intercalated isolated Pd may benefit the charge transfer in bulk C_3N_4. Moreover, the Pd 3*d* profiles (Supplementary Figure 5a) of 3Pd/C_3N_4 and 0.5Pd/C_3N_4 can be deconvolved into two pairs of doublets with $3d_{5/2}$ positions at 335.8 and 337.9 eV, $3d_{3/2}$ positions at 341.1 and 343.2 eV, which are assigned to metallic Pd^0 and oxidized $Pd^{\sigma+}$, respectively[39]. Compared with 3Pd/C_3N_4 and 0.5Pd/C_3N_4, few signals for Pd^0 existed in atomic 0.1Pd/C_3N_4 before or after Ar^+ etching (also verified by the DFT results in Supplementary Table 4), which indicates that the electronic structure of atomic 0.1Pd/C_3N_4 is different from those catalysts with high loading amount of Pd. It should be noted that both metallic Pd^0 and oxidized $Pd^{\sigma+}$ were detected on the surface of single-atom Pd/C_3N_4 without Ar^+ etching by Cao et al.[15] which is different from the results in our study. This distinction may contribute to the different preparation approach, leading to different surface properties of materials. The UV-vis spectra in supplementary Figure 6 indicates that grafting single atomic Pd to the structure of C_3N_4 has little effect on the light harvest of C_3N_4.

Catalytic mechanism. We further conducted DFT calculations in order to explore the possible photocatalytic mechanism of water splitting on *x*Pd/C_3N_4. For comparison, we choose the models of pristine C_3N_4 and C_3N_4 loaded with isolated Pd atom (Pd_1/C_3N_4) and Pd_6 cluster (Pd_6/C_3N_4) to investigate the size effect of Pd on the photocatalytic H_2 evolution performance. The charge densities of highest occupied molecular orbital/lowest unoccupied molecular orbital (HOMO/LUMO) and the alignments of HOMO/LUMO of C_3N_4, Pd_1/C_3N_4, and Pd_6/C_3N_4 are shown in Fig. 3 to compare their separation of electron and hole excited by light. The coordinates of Pd_1/C_3N_4 and Pd_6/C_3N_4 are shown in Supplementary Data 1 and 2. The geometrical structures of hydrogen adsorption on Pd_1/C_3N_4 and Pd_6/C_3N_4 and Pd (111) are depicted in Fig. 4 to reveal the active sites for photocatalytic H_2 evolution, which may be influenced by size-effect of loaded Pd.

The optimized structures of catalysts are shown in Supplementary Figure 8. Our results reveal that the cavity of C_3N_4 can stabilize the atomic Pd and Pd_6 cluster, similar to previous

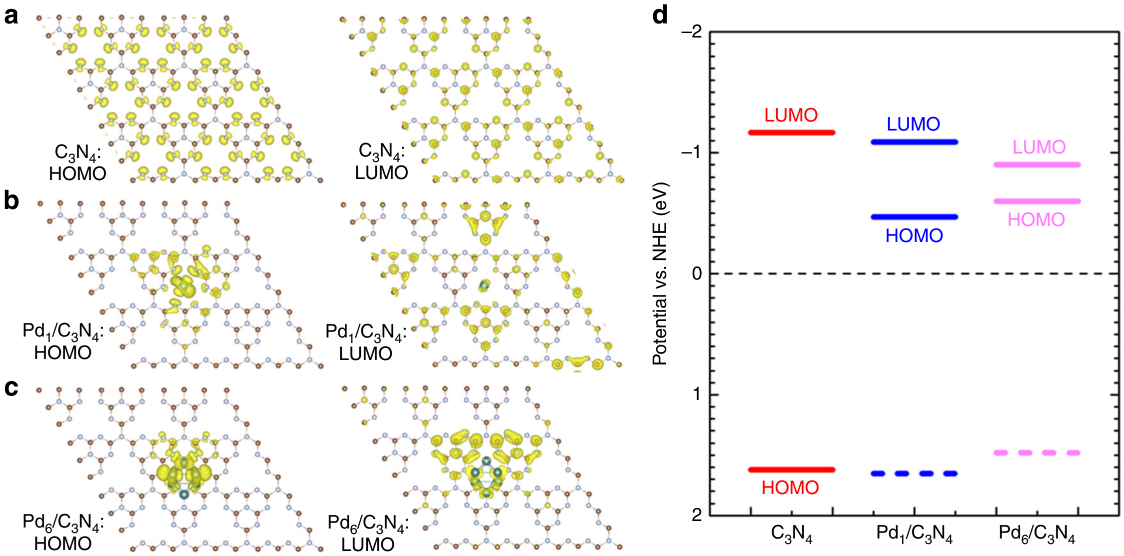

Fig. 3 Charge densities and band alignments of HOMO and LUMO. **a**–**c** The charge densities of HOMO/LUMO of C_3N_4, Pd_1/C_3N_4, and Pd_6/C_3N_4, respectively. The brown, gray, and olive spheres refer to carbon, nitrogen, and palladium atoms, respectively. The isovalue of the charge density is 0.01 e $(Å^3)^{-1}$. **d** The potentials vs. NHE of HOMO/LUMO of C_3N_4 (red line), Pd_1/C_3N_4 (blue line), and Pd_6/C_3N_4 (magenta line). The dash lines refer to the highest occupied orbital bellow the fermi level of C_3N_4 in Pd_1/C_3N_4 and Pd_6/C_3N_4

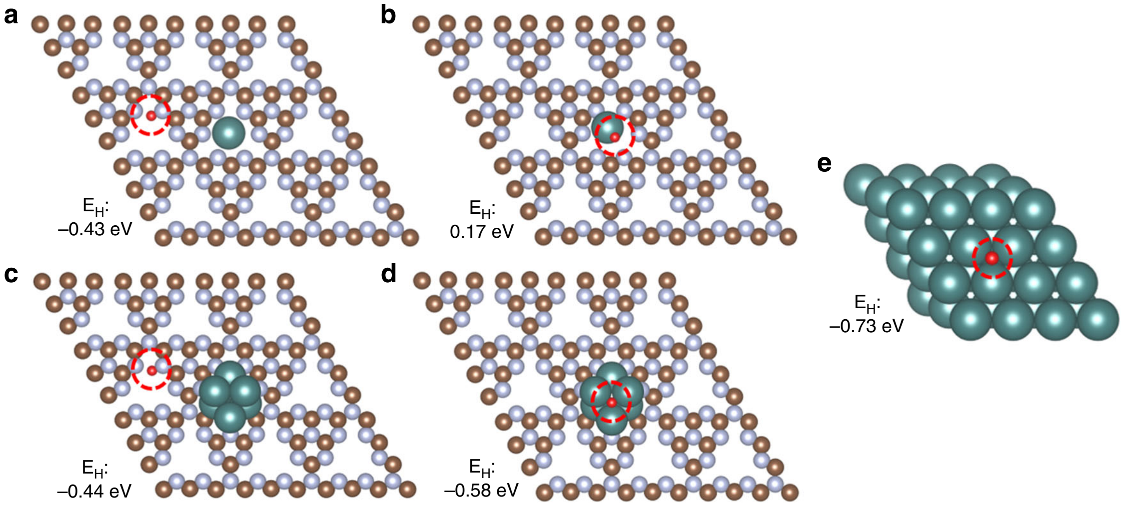

Fig. 4 Geometrical structures of hydrogen adsorption on Pd_1/C_3N_4, Pd_6/C_3N_4 and Pd (111) surface. Geometrical structures and adsorption energies of hydrogen adsorption on the **a** nitrogen and **b** palladium atoms in Pd_1/C_3N_4. Geometrical structures and adsorption energies of hydrogen adsorption on the **c** nitrogen atoms and **d** palladium cluster in Pd_6/C_3N_4. **e** Geometrical structure and adsorption energy of hydrogen adsorption on the palladium in Pd (111). The brown, gray, olive, and red spheres refer to the carbon, nitrogen, palladium, and hydrogen atoms, respectively. The adsorption sites of hydrogen are marked with red dash cycles

study[34]. After loading of Pd_1 or Pd_6, the band gap will decrease from 2.79 eV (pristine C_3N_4) to 0.58 eV (Pd_1/C_3N_4) and 0.30 eV (Pd_6/C_3N_4). The decrease of band gap is caused by the respectively electron states of Pd_1 and Pd_6 fill the band gap of C_3N_4 to improve the potential of valence band in Pd_1/C_3N_4 and Pd_6/C_3N_4 (details in Supplementary Figure 9). The distribution of charge density of HOMO and LUMO is studied since it is closely related to the activation behavior of photocatalyst. For pristine C_3N_4 (Fig. 3a), the HOMO mainly consists of charge densities from the edge N atoms in cavity of C_3N_4, and the LUMO consist of charge densities from the edge C atoms in cavities and the center graphitic N atoms in the C_3N_4 sheet. When C_3N_4 is loaded with Pd_1, the HOMO mainly consists of majority of charge densities from isolated Pd atom and very few charge densities from the C and N atoms interacting with Pd, and the LUMO mainly consists of charge densities from C and N atoms not interacting with Pd atom, within which some atoms are far from isolated Pd (Fig. 3b), indicating a strong spatial separation of electrons and holes. Similar to isolated Pd_1, the HOMO of Pd_6/C_3N_4 consists of majority of charge densities from Pd_6 cluster and the LUMO consists of charge densities from supporting C_3N_4 (Fig. 3c). Wang et al.[9] also reported the similar effect of O on the spatially separated HOMO and LUMO of C_3N_4. Therefore, the atomic-scale Pd loading on C_3N_4 will promote the separation of photogenerated electrons and holes while pristine C_3N_4 shows poor separation of electron–hole pairs when compared with the co-catalyst loaded with Pd.

The potentials of HOMO and LUMO versus NHE of pristine C_3N_4, Pd_1/C_3N_4, and Pd_6/C_3N_4 were also calculated and the results are shown in Fig. 3d. The potentials of HOMO and LUMO of CN are −1.17 and 1.62 eV, respectively, matching the previous study well[45]. With loading of Pd_1 and Pd_6, the potentials of HOMO decrease dramatically from 1.62 to −0.47 eV and −0.60 eV, respectively. The potentials of LUMO of Pd_1/C_3N_4 and Pd_6/C_3N_4 increase slightly from −1.17 to −1.09 eV and −0.90 eV, respectively. The potentials of calculated HOMO of supporting C_3N_4 without interaction with Pd atom are closed to the HOMO of pristine C_3N_4. The potential difference leads to the transfer of holes from the HOMO with high potential to the HOMO with low potential. The potentials of Pd_1 and Pd_6 are much smaller than that of the supporting C_3N_4, indicating that the photogenerated holes of C_3N_4 transfer to Pd_1 and Pd_6 and the electrons remain in C_3N_4. Considering the narrower bandgap of C_3N_4 after loaded with Pd, the visible triggered H_2 evolution reactions may mainly happen on the atomic Pd-loaded C_3N_4 over Pd_1/C_3N_4 catalyst.

Based on the study of optical activation behavior of Pd_1/C_3N_4, and Pd_6/C_3N_4, we found that the electrons will accumulate in supporting C_3N_4 and holes will accumulate in Pd atoms. Then, we turn to the study of hydrogen adsorption on Pd_1/C_3N_4 and Pd_6/C_3N_4. There are many adsorption sites that we took into consideration, such as Pd_1 and Pd_6, hole of C_3N_4 with or without loading of Pd_1 and Pd_6 (details in Supplementary Figure 10). Inspired by the above conclusion that the supporting C_3N_4 of the co-catalysts is the accumulation site of electrons, which is the most possible reactive site for hydrogen evolution, so the hydrogen adsorption energies on the supporting C_3N_4 and the loaded Pd_1, Pd_6, and Pd (111) (represent the large Pd particle) are studied and the most stable structures of hydrogen adsorption are summarized in Fig. 4. As shown in Fig. 4a, the most stable adsorption site of hydrogen on Pd_1/C_3N_4 is pyridine N in the C_3N_4 cavity adjoining Pd-loaded cavity rather than the isolated Pd atom (−0.43 vs. 0.17 eV). It is worth to note that the adsorption of hydrogen on the cavity of C_3N_4 without loading of Pd_1 is much stronger than that with loading of Pd_1 (Supplementary Figure 10). In Pd_1/C_3N_4, the cavity of C_3N_4 adjoining Pd_1-loaded cavity is the ground-stable adsorption site of hydrogen and accumulation site of activated electrons simultaneously. This is the reason why Pd_1/C_3N_4 possesses the excellent photocatalytic H_2 evolution performance. For Pd_6/C_3N_4 (in Fig. 4b), the size increase of atomic-scale Pd will enhance the adsorption ability of hydrogen, so the adsorption of hydrogen on Pd_6 is stronger than that on supporting C_3N_4 (−0.58 vs. −0.44 eV). For large Pd particle, the stable Pd (111) are used to simulate its surface behavior and adsorption of hydrogen will further be enhanced when comparing with Pd_6 cluster (−0.73 vs. −0.58 eV). When the size of atomic-scale Pd increases, the hydrogen atom prefers to be adsorbed on Pd clusters instead of supporting C_3N_4, which is the accumulation site of activated electrons. Therefore, the large size of atomic-scale Pd is harmful to the improvement of photocatalytic H_2 evolution performance of co-catalyst. Our work interprets a distinct active site for H_2 evolution route with those reported routes on noble metals for H_2 evolution (photoinduced electrons transfer from semiconductor to metal and then reduce H^+ to hydrogen molecules)[7,32,46–50]. These interesting results reveal that the size effect of noble metal could affect the active sites for H_2 evolution and present new insights into the roles of pyridine N in the cavities of C_3N_4 with decorated heteroatoms in H_2 evolution process, which may give inspiration for designing atomic catalysts for water splitting.

Discussion

In summary, single-atom Pd is successfully prepared and stably located in the six-fold cavity of C_3N_4. The distinctly different element constitutes of energy bands of the $0.1Pd/C_3N_4$ give intrinsic character of catalyst for the charge separation. The separation of photoinduced charges on $0.1Pd/C_3N_4$ is more like a semiconductor/semiconductor composite catalyst (C_3N_4 unites near atomic Pd is composited with those C_3N_4 units far away from atomic Pd): photoinduced electron–hole pairs from C_3N_4 units will transfer to the C_3N_4 units interacting with atomic Pd and be separated; most importantly, C_3N_4 units interacting with atomic Pd can utilize the long wave visible light to generate hot electrons; on the C_3N_4 units near atomic Pd, H ions adsorb on pyridine N atoms in the C_3N_4 cavities adjoining Pd-loaded cavity and are reduced by electrons and then desorb as H_2 molecules. The H_2 evolution on C_3N_4 can be greatly boosted by loading atomic Pd resulting from the appropriate sites for hydrogen adsorption, as well as accumulation of photoinduced electrons. This work provides new fundamental insights into the roles of pyridine N atoms in the cavities of C_3N_4 with decorated heteroatoms in H_2 evolution process and extends the photocatalytic H_2 evolution mechanism of C_3N_4 materials, which is expected to give inspiration for investigating atomic catalysts for water splitting on which the reaction mechanism may be distinct with those on nanoparticle or cluster-based catalysts, as well as designing high-performance catalysts for H_2 evolution.

Methods

Catalyst preparation. C_3N_4 was prepared via thermal condensation of urea. In detail, urea was placed in a closed alumina crucible, then it was heated to 600 °C in a muffle with a heating rate of 2 °C/min and held in this temperature for 4 h in air. After cooling it to room temperature, the as-obtained yellowish product was ground into fine powder with an agate mortar. The Pd/C_3N_4 were synthesized using a facile liquid-phase adsorption method as follows: The as-prepared C_3N_4 (0.5 g) was firstly suspended in 50 ml ultrapure water and sonicated for 60 min, then to gain various Pd loading content hybrid Pd/C_3N_4 (0.05, 0.1, 0.5, 3 wt%), a certain volume of H_2PdCl_4 (0.01 M) solution was added into the C_3N_4 aqueous dispersion and then sonicated mixed again for 60 min. Subsequently, in order to adjust the pH up to 9, appropriate Na_2CO_3 (0.1 M) was added into the mixed solution dropwise and slowly, after stirring for 18 h, the resultant product was washed with a large amount of ultrapure water for several times and further dried in an 60 °C oven overnight. The final obtained samples were labeled as $0.05Pd/C_3N_4$, $0.1Pd/C_3N_4$, $0.5Pd/C_3N_4$, and $3Pd/C_3N_4$, respectively. All as-prepared catalysts were reduced under H_2 atmosphere at 473 K for 1 h before characterization.

Characterization. The X-ray powder diffraction (XRD) patterns were performed on a D/max-RB X-ray diffractometer (Rigaku, Japan) with a Cu Kα radiation source ($\lambda = 1.54065$ Å, 40 kV, 100 mA), operating at a scanning angle range of 10–80° (5 °C/min). The nitrogen adsorption and desorption isotherms were conducted on a Micrometrics ASAP 2020 instrument. The Brunauer–Emmett–Teller (BET) surface area was obtained by a multipoint BET method using adsorption data in the relative pressure (P/P_0) range of 0.05−0.25. Transmission electron microscopy (TEM) and high-angle annular dark-field STEM (HAADF-STEM) were used to identify the morphological and structure features. The HAADF-STEM images were achieved by a FEI Tecnai G2 F30 HR-TEM/STEM microscope (Japan) and operating at an accelerating voltage of 200 kV. XPS were measured on a Physical Electronics PHI5802 X-ray spectrometer with Mg Kα X-ray (Kα = 1253.6 eV) as excitation source and using the C 1s peak of adventitious carbon (284.8 eV) for calibration. The metal loading concentrations were determined by ICP-AES on a Shimadzu Corporation-ICP-7500 instrument. UV–visible diffuse reflectance spectra were recorded using a Shimadzu UV–vis S-4100 spectrophotometer equipped with an integrated sphere, using $BaSO_4$ powder as reflectance material over the wavelength range of 200–800 nm. The photocurrents and EIS measurements were recorded on an electrochemical analyzer (CHI 750D Instruments) with a standard three-electrode system using the samples coated on fluorine-doped tin oxide (FTO) glass as the working electrodes, a Pt foil as the counter electrode, and Ag/AgCl (saturated KCl) as a reference electrode. The light was provided by a 300 W Xe arc lamp. The working electrodes were prepared as follows: 10 mg of photocatalyst was dispersed in a mixture of 200 μl of isopropanol and 20 μl of Nafion to make a slurry. A 30 μl portion of the slurry was then coated onto a 1 cm^{-2} FTO conductive glass and dried to form working electrode. The ultrafast TA measurements were performed under ambient conditions, on a Helios pump-probe system (Ultrafast Systems LLC) in combination with an amplified femtosecond laser system (Coherent). The 400-nm pump pulses (~100 nJ/pulse at the sample) were delivered by an optical parametric amplifier (TOPAS-800-fs), which was excited by a Ti:sapphire regenerative amplifier (Legend Elite-1K-HE; center wavelength 800 nm, pulse duration 35 fs, pulse energy 3 mJ, repetition rate 1 kHz) seeded with a mode-locked Ti:sapphire laser system (Micra 5) and pumped with a 1-kHz Nd:YLF laser (Evolution 30). The stable white-light continuum (WLC) probe pulses (450–650 nm for this work) were generated by focusing the 800-nm beam (split from the regenerative amplifier, ~400 nJ/pulse) onto a sapphire crystal plate. A reference beam split from the WLC was used to correct the pulse-to-pulse fluctuation of the WLC. The time delays between the pump and probe pulses were varied by a motorized optical delay line. The instrument response function (IRF) was determined to be ~100 fs by cross-correlating the pump and probe pulses at the sample. A mechanical chopper operating at 500 Hz was used to modulate the pump pulses such that the TA spectra with and without the pump pulses can be recorded alternately. The temporal and spectral profiles (chirp corrected) of the pump-induced differential transmission of the WLC probe light (i.e., absorbance change, ΔA) were visualized by an optical fiber-coupled multichannel spectrometer (with a CMOS sensor) and further processed by the Surface Xplorer software equipped with the Helios system. The samples well dispersed in pure ethylene glycol were contained in a 0.7 mL sealed quartz cuvette under a continuous magnetic stirring condition ensuring that the photoexcited volume of the sample was kept fresh during the TA measurements. Fourier transform infrared spectroscopic (FTIR, Thermo Scientific Nicolet IS50, USA) of CO adsorption was performed to determine the initial states of Pd species. The spectra of CO adsorption at 298 K were recorded after the sample was exposed to CO (1 vol%) balanced by N_2 (100 ml min^{-1}) for more than 0.5 h and then purged with a N_2 flow (100 ml min^{-1}) for 40 min to remove the weak adsorbed CO. The spectra of CO adsorption were recorded each 10 min until reaching saturated CO adsorption state.

Photocatalytic performance and durability test. Visible-light-driven H_2 evolution were conducted in a gas-closed circulation system equipped with a vacuum line. In detail, 100 mg sample powder was suspended in 100 ml 20 vol% triethanolamine (TEOA) aqueous solution and vacuumed for 30 min to remove dissolved oxygen in the mixed aqueous solutions before evaluation. Visible light radiation was provided by a 300 W Xe lamp (Ceaulight) with a UV-CUT filter ($\lambda > 400$ nm). The relative focused intensity is about 180 mW cm^{-2}. To keep the catalyst powders suspended in the mixed solutions uniformly, continuous stirring was applied during the reaction of water splitting driven by visible light. The generated H_2 was determined by an online gas chromatography (Ceaulight, GC7920, 5 Å molecular sieve columns, N_2 carrier) equipped with a thermal-conductivity detector (TCD). The photocatalytic H_2 generation durability was characterized by performing four cycle runs with each 4 h under similar conditions.

Computational methods and details. All density-functional theory (DFT) calculations in this study were implemented by the Vienna Ab initio Simulation Package (VASP)[51,52]. The projected augmented wave (PAW) potential[53,54] was employed to describe the electron–ion interactions. When optimizing the geometric structures, the generalized gradient approximation (GGA) method[55] with the Perdew−Burke−Ernzerhof (PBE) functional[56] and vdW correction based on DFT-D3 method[57] was applied to describe the exchange-correlation energy. The cutoff energy for plane wave basis was set to 400 eV, and the convergence criteria of energy is 10^{-5} eV. Due to the poor results of band gap energies for semiconductors calculated by the PBE method, the hybrid functional (HSE06)[58] was applied to the electronic structure calculations (Supplementary Figure 7). To obtain the correct band gap energies, the cutoff energy was increased to 520 eV. The optimized lattice parameter of C_3N_4 unit cell was 7.13*7.13*16 Å, which consistent with previous result[59].

The 3*3 supercell of C_3N_4 was built to the stable adsorption structures of Pd_1/C_3N_4 and Pd_6/C_3N_4 and relative hydrogen adsorption morphologies. The vacuum slab perpendicular to the C_3N_4 surface was set to the 15 Å to avert the interaction between the periodic layers. The Brillouin zone is sampled with a single gamma-centered Monkhost–Pack mesh. All the structures were fully relaxed until the force on each atom was less than 0.01 eV $Å^{-1}$.

Data availability

Data that related to the findings of this paper are available from the corresponding author upon reasonable request.

Received: 8 August 2018 Accepted: 21 January 2019

References

1. Lewis, N. S. Toward cost-effective solar energy use. *Science* **315**, 798–801 (2007).
2. Lewis, N. S. & Nocera, D. G. Powering the planet: chemical challenges in solar energy utilization. *Proc. Natl Acad. Sci. USA* **103**, 15729–15735 (2006).
3. Seh, Z. W. et al. Combining theory and experiment in electrocatalysis: insights into materials design. *Science* **355**, 1–12 (2017).
4. Kudo, A. & Miseki, Y. Heterogeneous photocatalyst materials for water splitting. *Chem. Soc. Rev.* **38**, 253–278 (2009).
5. Hisatomi, T., Kubota, J. & Domen, K. Recent advances in semiconductors for photocatalytic and photoelectrochemical water splitting. *Chem. Soc. Rev.* **43**, 7520–7535 (2014).
6. Hu, J. et al. A versatile strategy for shish-kebab-like multi-heterostructured chalcogenides and enhanced photocatalytic hydrogen evolution. *J. Am. Chem. Soc.* **137**, 11004–11010 (2015).
7. Fujishima, A. & Honda, K. Electrochemical photolysis of water at a semiconductor electrode. *Nature* **238**, 37–38 (1972).
8. Wang, X. et al. A metal-free polymeric photocatalyst for hydrogen production from water under visible light. *Nat. Mater.* **8**, 76–80 (2009).
9. Wang, Y. et al. Linker-controlled polymeric photocatalyst for highly efficient hydrogen evolution from water. *Energy Environ. Sci.* **10**, 1643–1651 (2017).
10. Wang, Y., Wang, X. & Antonietti, M. Polymeric graphitic carbon nitride as a heterogeneous organocatalyst: from photochemistry to multipurpose catalysis to sustainable chemistry. *Angew. Chem. Int. Ed.* **51**, 68–89 (2012).
11. Zhang, Y. & Antonietti, M. Photocurrent generation by polymeric carbon nitride solids: an initial step towards a novel photovoltaic system. *Chem. Asian J.* **5**, 1307–1311 (2010).
12. Liu, J. et al. Metal-free efficient photocatalyst for stable visible water splitting via a two-electron pathway. *Science* **347**, 970–974 (2015).
13. Ong, W. J., Tan, L. L., Ng, Y. H., Yong, S. T. & Chai, S. P. Graphitic carbon nitride (g-C_3N_4)-based photocatalysts for artificial photosynthesis and environmental remediation: are we a step closer to achieving sustainability? *Chem. Rev.* **116**, 7159–7329 (2016).
14. Yang, J., Wang, D., Han, H. & Li, C. Roles of cocatalysts in photocatalysis and photoelectrocatalysis. *Acc. Chem. Res.* **46**, 1900–1909 (2013).
15. Cao, S. et al. Single-atom engineering of directional charge transfer channels and active sites for photocatalytic hydrogen evolution. *Adv. Funct. Mater.* **28**, 1802169 (2018).
16. Deng, J. et al. Triggering the electrocatalytic hydrogen evolution activity of the inert two-dimensional MoS_2 surface via single-atom metal doping. *Energy Environ. Sci.* **8**, 1594–1601 (2015).
17. Kwak, J. et al. Coordinatively unsaturated Al^{3+} centers as binding sites for active catalyst phases of platinum on γ-Al_2O_3. *Science* **325**, 1670–1673 (2009).
18. Valden, M., Lai, X. & Goodman, D. Onset of catalytic activity of gold clusters on titania with the appearance of nonmetallic properties. *Science* **281**, 1647–1650 (1998).
19. Zhao, Y. et al. Stable iridium dinuclear heterogeneous catalysts supported on metal-oxide substrate for solar water oxidation. *Proc. Natl Acad. Sci. USA* **115**, 2902–2907 (2018).
20. Lin, J. et al. Remarkable performance of Ir_1/FeO_x single-atom catalyst in water gas shift reaction. *J. Am. Chem. Soc.* **135**, 15314–15317 (2013).
21. Shan, J., Li, M., Allard, L. F., Lee, S. & Flytzani-Stephanopoulos, M. Mild oxidation of methane to methanol or acetic acid on supported isolated rhodium catalysts. *Nature* **551**, 605–608 (2017).
22. Liu, P. et al. Photochemical route for synthesizing atomically dispersed palladium catalysts. *Science* **352**, 797–800 (2016).
23. Yan, H. et al. Single-atom Pd_1/graphene catalyst achieved by atomic layer deposition: remarkable performance in selective hydrogenation of 1,3-butadiene. *J. Am. Chem. Soc.* **137**, 10484–10487 (2015).
24. Xie, S. et al. Atomic layer-by-layer deposition of Pt on Pd nanocubes for catalysts with enhanced activity and durability toward oxygen reduction. *Nano Lett.* **14**, 3570–3576 (2014).
25. Ding, K. et al. Identification of active sites in CO oxidation and water-gas shift over supported Pt catalysts. *Science* **350**, 189–192 (2015).
26. Yang, X. et al. Single-atom catalysts: a new frontier in heterogeneous catalysis. *Acc. Chem. Res.* **46**, 1740–1748 (2013).
27. Gates, B. C., Flytzani-Stephanopoulos, M., Dixon, D. A. & Katz, A. Atomically dispersed supported metal catalysts: perspectives and suggestions for future research. *Catal. Sci. Technol.* **7**, 4259–4275 (2017).
28. Xing, J. et al. Stable isolated metal atoms as active sites for photocatalytic hydrogen evolution. *Chem. Eur. J.* **20**, 2138–2144 (2014).
29. Yang, M. et al. Catalytically active Au-O$(OH)_x$-species stabilized by alkali ions on zeolites and mesoporous oxides. *Science* **346**, 1498–1501 (2014).
30. Li, F., Li, Y., Zeng, X. & Chen, Z. Exploration of high-performance single-atom catalysts on support M_1/FeO_x for CO oxidation via computational study. *ACS Catal.* **5**, 544–552 (2015).
31. Cheng, N. et al. Platinum single-atom and cluster catalysis of the hydrogen evolution reaction. *Nat. Commun.* **7**, 13638 (2016).

32. Li, X. et al. Single-atom Pt as co-catalyst for enhanced photocatalytic H_2 evolution. *Adv. Mater.* **28**, 2427–2431 (2016).
33. Vile, G. et al. A stable single-site palladium catalyst for hydrogenations. *Angew. Chem. Int. Ed.* **54**, 11265–11269 (2015).
34. Gao, G., Jiao, Y., Waclawik, E. R. & Du, A. Single atom (Pd/Pt) supported on graphitic carbon nitride as an efficient photocatalyst for visible-light reduction of carbon dioxide. *J. Am. Chem. Soc.* **138**, 6292–6297 (2016).
35. Gao, G. P. et al. Metal-free graphitic carbon nitride as mechano-catalyst for hydrogen evolution reaction. *J. Catal.* **332**, 149–155 (2015).
36. Liu, J., Zhang, T., Wang, Z., Dawson, G. & Chen, W. Simple pyrolysis of urea into graphitic carbon nitride with recyclable adsorption and photocatalytic activity. *J. Mater. Chem.* **21**, 14398–14401 (2011).
37. Han, C. et al. Formation and characterization of PdZn Alloy: a very selective catalyst for alkyne semihydrogenation. *J. Phys. Chem. C* **115**, 8457–8465 (2011).
38. Priolkar, K. R. et al. Formation of $Ce_{1-x}PdxO_{2-\sigma}$ solid solution in combustion-synthesized Pd/CeO_2 catalyst: XRD, XPS and EXAFS investigation. *Chem. Mater.* **14**, 2120–2128 (2002).
39. Arrigo, R. et al. Nature of the N–Pd interaction in nitrogen-doped carbon nanotube catalysts. *ACS Catal.* **5**, 2740–2753 (2015).
40. Bulushev, D. A. et al. Single isolated Pd^{2+} cations supported on N-doped carbon as active sites for hydrogen production from formic acid decomposition. *ACS Catal.* **6**, 681–691 (2016).
41. Levinson, R., Berdahl, P. & Akbari, H. Solar spectral optical properties of pigments—Part I: model for deriving scattering and absorption coefficients from transmittance and reflectance measurements. *Sol. Energy Mater. Sol. Cells* **89**, 319–349 (2005).
42. Han, C., Wu, L., Ge, L., Li, Y. & Zhao, Z. AuPd bimetallic nanoparticles decorated graphitic carbon nitride for highly efficient reduction of water to H_2 under visible light irradiation. *Carbon N. Y.* **92**, 31–40 (2015).
43. Bai, S., Jiang, J., Zhang, Q. & Xiong, Y. Steering charge kinetics in photocatalysis: intersection of materials syntheses, characterization techniques and theoretical simulations. *Chem. Soc. Rev.* **44**, 2893–2939 (2015).
44. Zhang, Q. & Luo, Y. Probing the ultrafast dynamics in nanomaterial complex systems by femtosecond transient absorption spectroscopy. *High. Power Laser Sci. Eng.* **4**, e22 (2016).
45. Dong, F. et al. In situ construction of $g\text{-}C_3N_4/g\text{-}C_3N_4$ metal-free heterojunction for enhanced visible-light photocatalysis. *ACS Appl. Mater. Interfaces* **5**, 11392–11401 (2013).
46. Subbaraman, R. et al. Enhancing hydrogen evolution activity in water splitting by tailoring $Li^{+}\text{-}Ni(OH)_2\text{-}Pt$ Interfaces. *Science* **334**, 1256–1260 (2011).
47. Pan, Z., Zheng, Y., Guo, F., Niu, P. & Wang, X. Decorating CoP and Pt nanoparticles on graphitic carbon nitride nanosheets to promote overall water splitting by conjugated polymers. *ChemSusChem* **10**, 87–90 (2017).
48. Xiao, J. et al. Boosting photocatalytic hydrogen production of a metal-organic framework decorated with platinum nanoparticles: the platinum location matters. *Angew. Chem. Int. Ed.* **55**, 9389–9393 (2016).
49. Zhang, G., Lan, Z. A., Lin, L., Lin, S. & Wang, X. Overall water splitting by Pt/$g\text{-}C_3N_4$ photocatalysts without using sacrificial agents. *Chem. Sci.* **7**, 3062–3066 (2016).
50. Yu, J., Qi, L. & Jaroniec, M. Hydrogen production by photocatalytic water splitting over Pt/TiO_2 nanosheets with exposed (001) facets. *J. Phys. Chem. C.* **114**, 13118–13125 (2010).
51. Kresse, G. F. J. Efficiency of ab-initio total energy calculations for metals and semiconductors using a plane-wave basis set. *Comput. Mater. Sci.* **6**, 15–50 (1996).
52. Kresse, G. F. J. Efficient iterative schemes for ab initio total-energy calculations using a plane-wave basis set. *Phys. Rev. B* **54**, 11169–11186 (1996).
53. Blöchl, P. E. Projector augmented-wave method. *Phys. Rev. B* **50**, 17953–17979 (1994).
54. Kresse, G. J. & From, D. ultrasoft pseudopotentials to the projector augmented-wave method. *Phys. Rev. B* **59**, 1758–1775 (1999).
55. Perdew, J. P., Burke, K. & Ernzerhof, M. Generalized gradient approximation made simple. *Phys. Rev. Lett.* **77**, 3865–3868 (1996).
56. Perdew, J. P., Ernzerhof, M. & Burke, K. Rationale for mixing exact exchange with density functional approximations. *J. Chem. Phys.* **105**, 9982–9985 (1996).
57. Grimme, S. Semiempirical GGA-type density functional constructed with a long-range dispersion correction. *J. Comput. Chem.* **27**, 1787–1799 (2006).
58. Heyd, J., Scuseria, G. E. & Ernzerhof, M. Hybrid functionals based on a screened coulomb potential. *J. Chem. Phys.* **118**, 8207–8215 (2003).
59. Ma, X. et al. A strategy of enhancing the photoactivity of $g\text{-}C_3N_4$ via doping of nonmetal elements: a first-principles study. *J. Phys. Chem. C* **116**, 23485–23493 (2012).

Acknowledgements

The authors acknowledge support from the National Key Research and Development Program of China (2016YFC0700902-3, 2016YFA0200602, 2017YFB0701600, 2018YFA0208702), Shenzhen Projects for Basic Research (JCYJ20170817161720484, JCYJ20170412171430026), the National Natural Science Foundation of China (11874036, 21573211, 21633007), the local Innovative and Research Teams Project of Guangdong Pearl River Talents Program (2017BT01N111), and the Fundamental Research Funds for the Central Universities (WK2340000063).

Author contributions

L.L. contributed to the experimental process and paper-writing. X.W. contributed to the DFT calculations and helped the result analysis. L.W. conducted the Ultrafast spectroscopy characterizations helped the result analysis. X.X. conceived the research, L.G. performed the HAADF-STEM characterizations. Z.Si, J.L., and Q.Z. helped to discuss the performance results. Y.L. helped the TEM examination. Y.Z. helped the data analysis of EXAFS result. R.R., X.W., D.W., and F.K. provided test platform.

Additional information

Supplementary information accompanies this paper at https://doi.org/10.1038/s42004-019-0117-4.

Competing interests: The authors declare no competing interests.

Reprints and permission information is available online at http://npg.nature.com/reprintsandpermissions/

Publisher's note: Springer Nature remains neutral with regard to jurisdictional claims in published maps and institutional affiliations.